Quantitative Analysis of the Local Phase Transitions Induced by Laser Heating

Anton V. Ievlev[1,2,*], Michael A. Susner[3], Michael A. McGuire[3], Petro Maksymovych[1,2] and Sergei V. Kalinin[1,2]

[1]The Center for Nanophase Materials Sciences, Oak Ridge National Laboratory, 1 Bethel Valley Rd., Oak Ridge, TN 37831

[2]Institute for Functional Imaging of Materials, Oak Ridge National Laboratory, 1 Bethel Valley Rd., Oak Ridge, TN 37831

[3]Materials Science and Technology Division, Oak Ridge National Laboratory, 1 Bethel Valley Rd., Oak Ridge, TN 37831

*Author to whom correspondence should be addressed. Email: ievlevav@ornl.gov

Abstract

Functional imaging enabled by scanning probe microscopy (SPM) allows investigations of nanoscale material properties under a wide range of external conditions, including temperature. However, a number of shortcomings preclude the use of the most common material heating techniques, thereby limiting precise temperature measurements. Here we discuss an approach to local laser heating on the micron-scale and its applicability for SPM. We applied local heating coupled with piezoresponse force microscopy and confocal Raman spectroscopy for nanoscale investigations of a ferroelectric-paraelectric phase transition in copper indium thiophosphate

layered ferroelectric. Bayesian linear unmixing applied to experimental results allowed extraction of the Raman spectra of different material phases and enabled temperature calibration in the heated region. The obtained results enable a systematic approach for studying temperature-dependent material functionalities in heretofore-unavailable temperature regimes.

Keywords: ferroelectric, domain structure, scanning probe microscopy, piezoresponse forcr microscopy, Raman spectroscopy, phase transition

Currently, scanning probe microscopy (SPM) and its numerous variants have emerged as powerful methods for probing the structure and functionality of matter on the nanoscale. Quickly following the development of atomic force microscopy[1] where the mapping of the surface topography with nanometer spatial resolution was finally realized, numerous advancements were found in SPM applications for the imaging of functional properties. The sensitivity of SPM with respect to force has been extended to enable mechanical characterization, including force-distance curve mapping,[2] atomic force acoustic microscopy[3] and ultrasonic microscopy.[4] Controlling the tip bias has enabled broad classes of electric measurements as exemplified by Kelvin Probe Force Microscopy[5,6] and Electrostatic Force Microscopies,[7,8] current measurements,[9,10] and Piezoresponse Force Microscopy.[11-14] Finally, the development and introduction of heated probes has enabled a broad range of thermal imaging methods.[15-17]

Further developments in SPM-based functional imaging include measuring these functionalities as a function of external parameters, including temperature[18-30] and humidity.[30-34] Numerous studies are devoted to temperature-dependent investigation of material properties from mechanical to magnetic.

Both global and local approaches with respect to temperature control are used in SPM. In the global approach, the sample is heated through a temperature stage. This technique introduces a number of shortcomings including limitations of the maximum achievable temperature and the presence of strong temperature gradients in the case of heating stage. A local heating approach utilizes special SPM tips with integrated heaters in Scanning Thermal microscopy (SThM).[15-17] Although it provides the most localized heating, the realization of the electrical modes in SThM is hampered by interference between the electric signals used for the measurements and for heating. Moreover, quantitative analysis and calibration of SThM is always non-trivial due to

strong dependence of the contact thermal resistance on the detailed mechanical and chemical structure of the tip-surface junction.

Here we combine laser heating with piezoresponse force microscopy (PFM)[12,13] and confocal micro-Raman spectroscopy to investigate the ferroelectric-paraelectric phase transitions and dynamics of the ferroelectric domain structure close to the Curie temperature in the copper indium thiophosphate ($Cu_{1-x}In_{1+x/3}P_2S_6$) layered ferroelectrics.[35-37] PFM measurements demonstrated significant changes of the domain structure at the high values of the irradiation power, which was attributed to the transition into the paraelectric phase. This assumption was confirmed by micro-Raman measurements, which demonstrated significant changes in spectra at higher values of the excitation laser power. Advanced statistical techniques (Principal component analysis and Bayesian linear unmixing) applied for systematic investigations of the Raman spectra allowed us to determine critical values of the laser power for a given sample and, along with numerical simulations of the temperature distribution, to make the temperature calibration in the irradiated region.

Results and discussion

Local heating was induced by excitation laser (Fig. 1a). The diode-pumped solid-state laser (λ = 532 nm) with power ranges from 100 μW to 3 mW was used to enable local heating and measure Raman spectra. Laser heating is well-known in the field of confocal Raman spectroscopy and used for thermal conductivity measurements.[39-41] In this approach, a focused laser heats a micrometer-sized region of the sample. This localization is still small enough to enable micro-Raman measurements and not large enough to affect cantilever properties. At the same time, the region being heated is much larger than the tip contact area, providing an almost

uniform temperature distribution in the probing region. However, how to determine the absolute value of temperature in this region remains an open question.

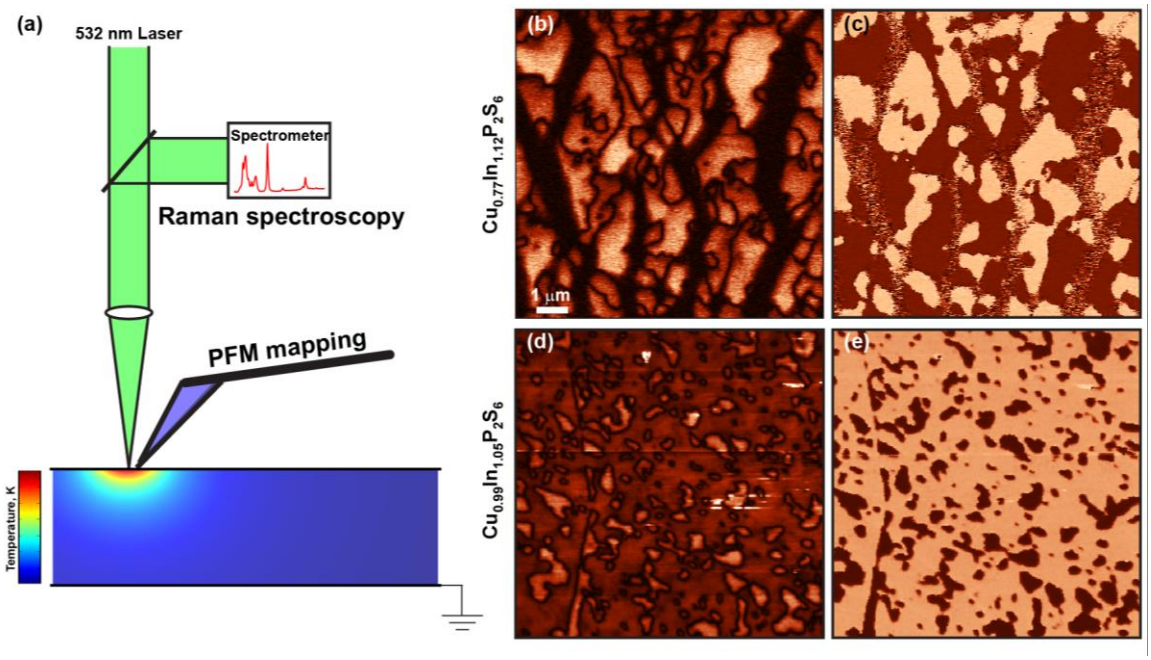

Figure 1. (a) Schematic representing experimental apparatus. PFM amplitude at room temperature (b,d) and phase (c,e) of the $Cu_{0.77}In_{1.12}P_2S_6$ and $Cu_{0.99}In_{1.05}P_2S_6$ samples, respectively.

The static domain structures of the CIPS samples were first studied by single-frequency piezoresponse force microscopy (PFM). In PFM, an AC electric field is applied to the sample through the conductive tip and leads to surface oscillations. Analysis of the amplitude and phase of these oscillations allows mapping of the spontaneous polarization direction under the tip with nanometer spatial resolution. In the general case, a phase contrast of 180^o should reveal ferroelectric antiparallel domains, while the amplitude contrast is mainly due to domain walls.[11-13]

Investigations showed the presence of a random domain structure, consisting of nanometer-sized domains with vertically directed polarization in both samples (Fig. 1b-e). Furthermore, the Cu-deficient sample $Cu_{0.77}In_{1.12}P_2S_6$ has extended nonpolar regions due to inclusions of centrosymmetric $In_{4/3}P_2S_6$ as discussed in detail in Ref.[38] These inclusions are clearly seen in the PFM amplitude signal, as regions of nearly zero piezoresponse (Fig. 1b).

Experiments with local heating induced by the laser focused near the SPM tip (Fig. 2) demonstrated a significant decrease of the piezoresponse amplitude at a laser excitation power above 900 μW in $Cu_{0.77}In_{1.12}P_2S_6$ (Fig. 2a-c). Reverting to lower laser power restored the initial piezoresponse contrast. However, the detailed spatial structure and distribution of the polarization domains also changed (compare Fig. 2d-e with Fig. 2f). These results along with proximity of the sample's T_c to room temperature[38] allowed us to assume that in applying a laser power of over 900 μW we had passed through the ferroelectric-paraelectric phase transition in the laser-irradiated region. As one can clearly see in Figure 2f, the changes in the domain structure restored after the cooling below Curie temperature are localized in the region corresponding to the maximum irradiation power. This fact confirms proper adjustment of the laser position with respect to the tip. At the same time PFM contrast doesn't show significant changes before and after heating, which confirms stability of the tip-surface junction properties.

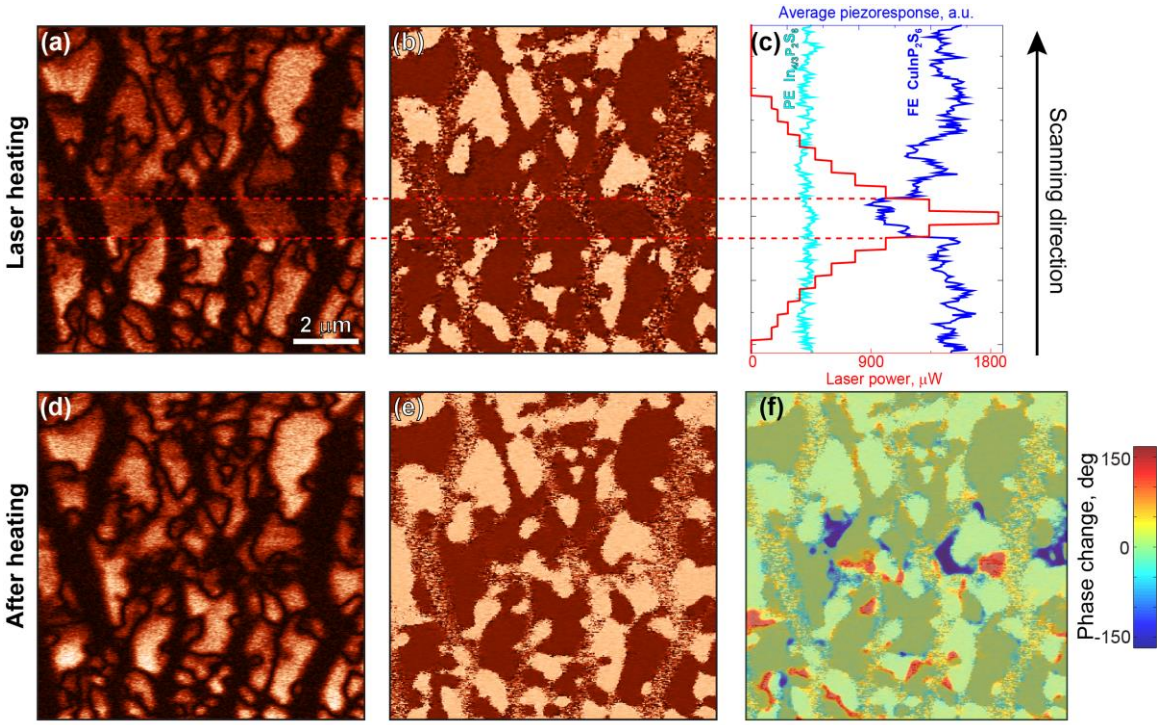

Figure 2. PFM mapping during and after laser heating in $Cu_{0.77}In_{1.12}P_2S_6$. (a) In-situ PFM measurements during heating with various laser intensities; we see the piezoresponse amplitude in (a) and the piezoresponse phase in (b). (c) Plot of laser power and average amplitude of the piezoresponse in ferroelectric $CuInP_2S_6$ and paraelectric $In_{4/3}P_2S_6$ phases. (d-e) Domain structure after heating; we see the piezoresponse amplitude in (d) and the piezoresponse phase in (e). (f) Heating induced changes in the domain structure elucidated by overlaying the phase signals from before and after heating.

To obtain further insight into local heating process, we performed finite element simulations of the temperature distribution and relaxation (Fig. 3a, b). We made these simulations by solving the classical isotropic heat transfer equation using the COMSOL Multiphysics software package. We fixed temperature to be equal to room temperature T_0 on the side and bottom boundaries of the sample (about 10 μm from the laser spot). We were not able to

locate published data regarding the thermal conductivity of CIPS, thus we used data for similar material – $Sn_2P_2S_6$: $\kappa \approx 0.6 Wm^{-1}K^{-1}$.[42] Although κ is expected to be a strongly anisotropic, as we study 2D layered material, in a first approximation we used isotropic model for rough temperature estimations.

The laser irradiation was simulated as a surface heat source with Gaussian distribution of heat density and integrated power $P_{source} = \alpha P_{laser}$, where P_{laser} is the power of the excitation laser and α is the laser adsorption efficiency which defines the portion of the laser energy converted into the heat. The FWHM of the distribution was set equal to laser spot size, R_{spot}. The average temperature was calculated over the Raman probing volume, a hemisphere with radius $R_{probing}$ = 500 nm.

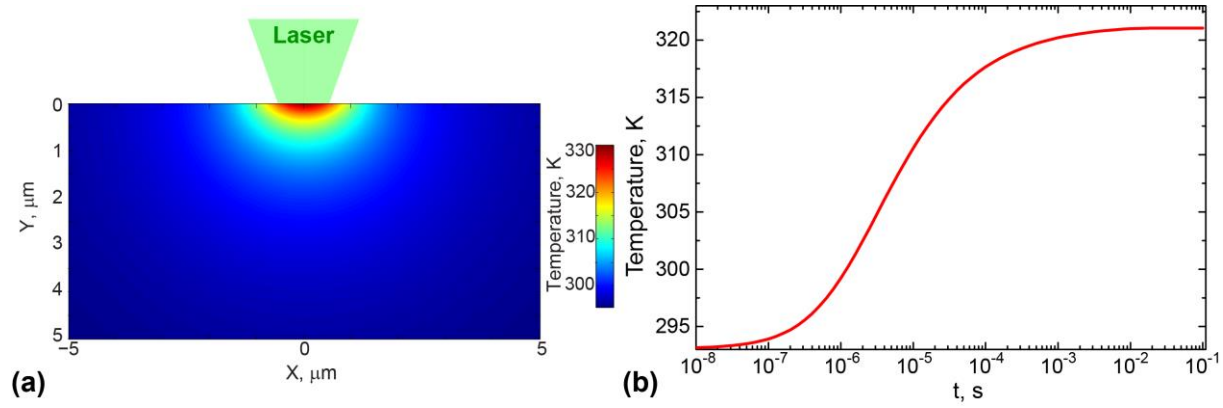

Figure 3. Finite element modeling of the local laser heating. (a) Temperature spatial distribution and (b) time relaxation.

The simulated spatial temperature distribution and time-relaxation are presented in figure 3a-b. Temperature relaxation time (Fig. 3b) was found to be much smaller than the typical SPM acquisition time (~ 1 ms), which enables stationary measurements. As expected, the heated region size is of the order of micrometers in both the lateral and vertical directions (Fig. 3a),

which is much larger than the typical contact area in SPM, but nevertheless comparable with the domain size. In addition, we found the temperature to be linearly proportional to the laser power, which can be used for calibration of the temperature absolute value.

We should note here that performed simulations do not take into account tip phenomena on the temperature distribution into the irradiated region (*e.g.* thermal conductivity, shadowing, *etc.*). However, this problem can be resolved by temperature calibration using macroscopically measured reference points (Curie temperatures).

To perform a temperature calibration, we utilized the fact that there exists a strong Raman spectral dependence with respect to the material phase. In this case, the temperature of the phase transition can be used as a reference point. However, the signals in the acquired Raman-spectroscopic dataset are found to be mixed due to temperature and material inhomogeneity. Unlike the PFM signals, collected from nanometer-sized regions with uniform temperature distributions, the optical signals comes from much larger areas (*i.e.* comparable to the beam size), resulting in mixed signals from the different phases.

To resolve this problem, we introduced statistical deconvolution methods, thus providing way to separate signals matched to the different phases. Confocal micro-Raman spectroscopic measurements with low laser excitation power (150 μW – well below critical power, determined by PFM) were performed in 7x7 μm regions with a resolution of 50x50 spatial points and 1650 spectral points. Typical Raman spectra, maps of in-situ PFM signals, and maps of integral Raman intensity are presented in Supplemental materials (Fig. S1).

One approach for the analysis of the data can be based on classical peak fitting by Gaussian, Lorentzian or Voigt profiles. This approach is not efficient and interpretation of its

output (fitting parameters maps) can be nontrivial, as it does not explicitly show relationships between peaks.

Statistical analysis using Principal Component Analysis (PCA) and Bayesian Linear Unmixing (BLU) provide an alternative method for the analysis of multidimensional datasets and detection of hidden patterns.[43-47] PCA allows linear decomposition of the multidimensional datasets on the superposition of orthogonal eigenvectors sorted by variability. In this case, spectral signals inside the dataset can be described by the few first eigenvectors and their spatial distribution by corresponding loading maps (detailed information is available in Supplemental materials).[45,46]

PCA is optimal for revealing of the hidden patterns and for determining their frequency. Results of the PCA on the Raman spectroscopic data from $Cu_{0.74}In_{0.26}P_2S_6$ can be found in Supplemental materials (Fig. S2). These data suggest the existence of at least two significant Raman contributions distributed over the scan. However, physical interpretation of the eigenvectors (Fig. S2a) in this case is hampered as they are constructed to be orthogonal and thus physically meaningless. Bayesian Linear Unmixing (BLU) can be performed to resolve this problem.

In the BLU algorithm,[43,44] the Raman spectrum for each spatial point X_i $(i = 1..N^2)$ is represented as a linear combination of number of independent positive endmembers (spectral components) v_j:

$$X_i = A_{ij} v_j + N_i \quad (1)$$

where abundance A_{ij} defines concentration of the j component in the i^{th} point and N_i is Gaussian noise. Two important constraints are incorporated: 1) non-negativity of endmembers and abundances (*i.e.* $A_{ij} > 0$ and $v_j > 0$) keeps these components physically meaningful and 2) the

additivity and sum-to-one $\sum_j A_{ij} = 1$ maintains total concentration in each point to be equal to one. The number of the components for unmixing is postulated by the researcher, and can be defined from the physical assumptions or other statistical methods (e.g. PCA).

In the general case, the measured optical signal *M* can be represented as a convolution of a probe resolution function *P* and real material response *R*.

$$M(x,y) = \int R(x-\tau_1, y-\tau_2) \cdot P(\tau_1, \tau_2) d\tau_1 d\tau_2 \quad (2)$$

In the case of linear combination of responses: $R = \sum_i \alpha_i r_i$, the measured signal represents a linear combination of convoluted functions m_i, which can be unmixed using BLU:

$$M(x,y) = \int \sum_i \alpha_i r_i (x-\tau_1, y-\tau_2) \cdot P(\tau_1, \tau_2) d\tau_1 d\tau_2 = \sum_i \int \alpha_i r_i (x-\tau_1, y-\tau_2) \cdot P(\tau_1, \tau_2) d\tau_1 d\tau_2 = \sum_i \alpha_i m_i \quad (3)$$

Imaging over multiple locations provides multiple realizations, and BLU is ideally matched for extraction of the unknown endmembers. Of course, it cannot perform spatial deconvolution, but it is able to provide Raman spectra corresponding to different phases. Spatial and beam inhomogeneity, which is a problem in the case of a single point measurements here becomes an asset, since it gives multiple realizations of response. Detailed description of the practical implementation of the blind Bayesian unmixing can be found in ref [[25,26]].

To illustrate this approach, we first demonstrate component unmixing in the (*x*,*y*) space. Results of the BLU of the $Cu_{0.77}In_{1.12}P_2S_6$ Raman data are presented for two components in Figure 3 and for three components in Supplemental materials (Fig. S3). As one can see, the best unmixing is achieved for two components (the last component in three component unmixing is noise-driven). Taking into account presence of the nonpolar $In_{4/3}P_2S_6$ inclusions (Fig. 1b,c) in the considered sample, unmixed components (Fig. 4c) can be attributed to Raman spectra of the ferroelectric-polar $CuInP_2S_6$ (Fig. 4b) and centrosymmetric-nonpolar $In_{4/3}P_2S_6$ (Fig. 4a) regions.

Strictly speaking, the Raman spectra can also be changed by strain and other phenomena, however, variation in this case is much weaker than between different phases, and hence this effect is only detectable in high-energy mapping.

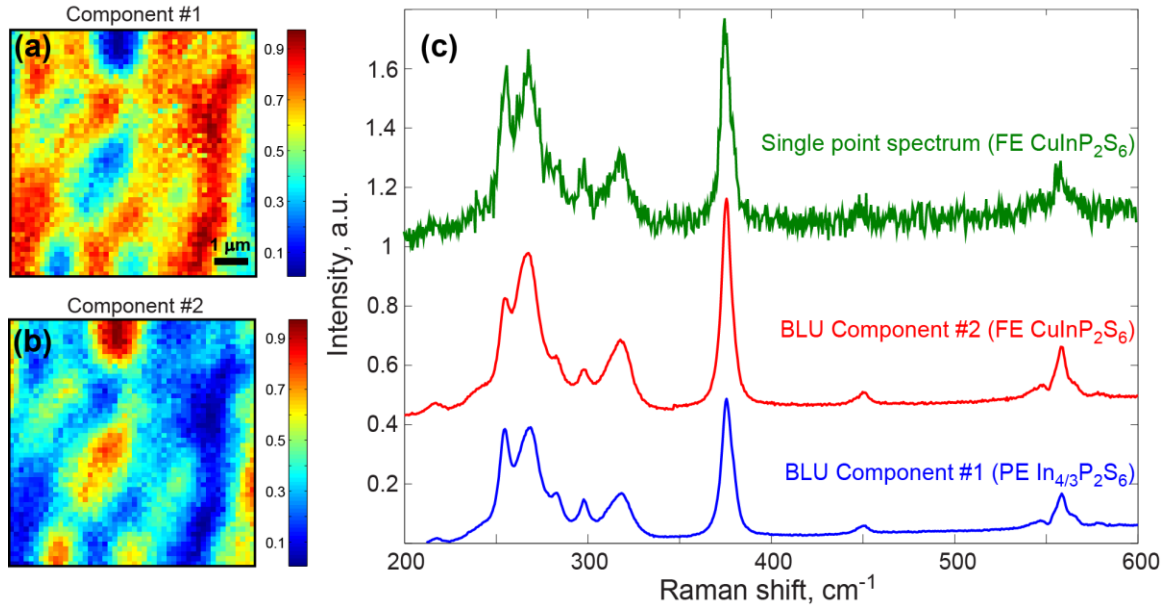

Figure 4. Room temperature BLU of Raman spectroscopic data of $Cu_{0.77}In_{1.12}P_2S_6$ into 2 components. Abundance maps (a,b) and corresponding endmember spectra (c). Attempts to unmix into more components give maps with spurious contrast that are unphysical (Suppl. Mat). This suggests that two is ideal number of components, as expected for two-phase linear mixture (*x*,*y* sampling).

We further utilize this approach to separation in (*x*, *y*, *T*) space, where material response is mapped as both a function of space and temperature. To do this we performed Raman spectral mapping with a gradual increase of the excitation laser power from 400 μW to 1.6 mW (Fig. 5a,b). Spectra averaged over the regions measured with same laser intensity (Fig. 5c) clearly demonstrate a change of the Raman spectra with increasing laser power. In addition to the

obvious increase in the spectral intensity, significant changes in the spectra shape can be found in the bands near 300 cm^{-1}, 450 cm^{-1} and 550 cm^{-1}. However, it is not quite easy to characterize the changes in the spectra *via* the phase transition, as it was demonstrated that the above sample consists of two physically different types of regions, each represented by different Raman spectra.

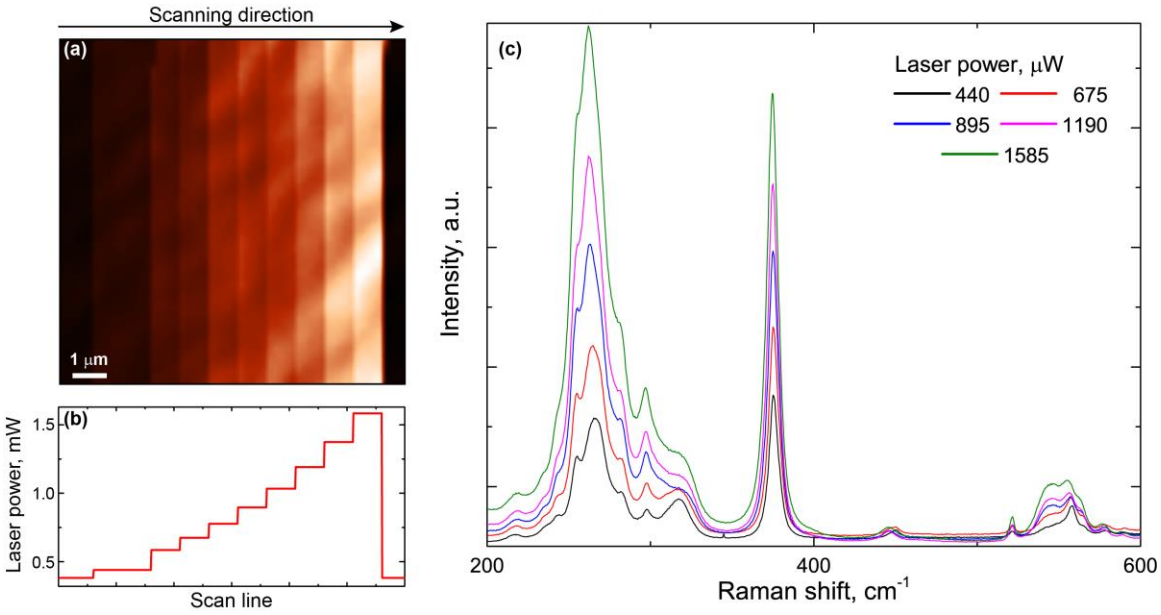

Figure 5. Raman spectra mapping of $Cu_{0.77}In_{1.12}P_2S_6$ with different intensities of laser power . (a) Map of the integral Raman intensity. (b) Plot of the laser power. (c) Raman spectra averaged over regions with fixed irradiation power.

However, BLU cannot be used on the raw Raman data, as it does not meet the normalization condition. This problem can be resolved by renormalization of the dataset to the power of the excitation laser. To assess quality of the data normalization we performed PCA over the normalized dataset (Supplemental materials, Fig. S4). Results demonstrate the presence

of a component which is independent on the laser power (Fig. 6a) which in turn corresponds to the temperature independent contribution to the convoluted Raman spectra (*i.e.* $In_{4/3}P_2S_6$).

Using an approach similar to the constant temperature data, we show that the best results of the Bayesian unmixing of the (*x, y, T*) spectra were achieved by unmixing into three components (Fig. 6). Non-polar $In_{4/3}P_2S_6$ inclusions are readily identified, mainly due to the lack of change in the Raman spectra for this compound in the investigated temperature regimes. In Figure 6a we label the deconvoluted Raman spectrum resulting from the $In_{4/3}P_2S_6$ phase as Component 1 (Fig 6a). The third (Fig. 6c) and second (Fig. 6b) components are mutually exclusive at high and low temperatures but do coexist in a narrow intermediate temperature range. Therefore, they can be attributed to ferroelectric $CuInP_2S_6$ (#3) and paraelectric $CuInP_2S_6$ above Curie temperature (#2). Corresponding Raman spectra (Fig. 6d) clearly demonstrate changes in bands near 300, 450 and 550 cm^{-1}. The comprehensive analysis of these changes along with identification of the Raman bands can give important information about crystallographic structure of CIPS and its changes near the phase transition, but is beyond the topic of this manuscript and will be published elsewhere.

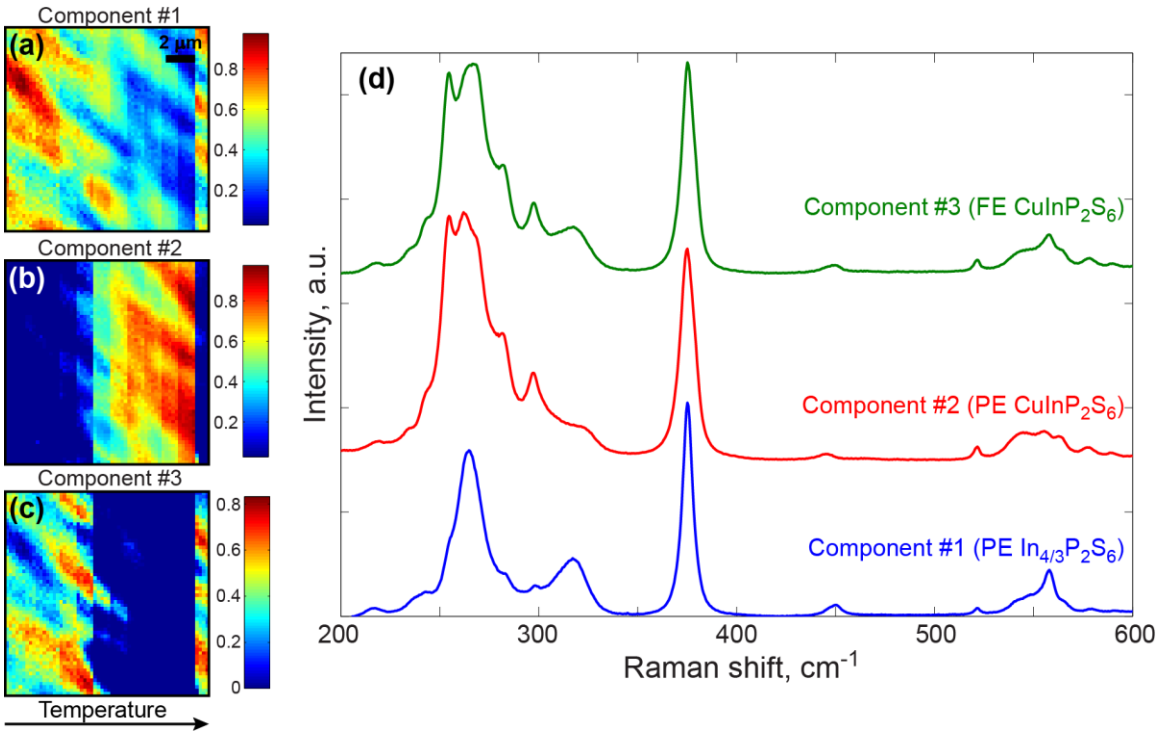

Figure 6. BLU of normalized Raman spectroscopic data of $Cu_{0.77}In_{1.12}P_2S_6$ (mapping with different values excitation laser power). Abundance maps (a-c) and corresponding endmember spectra (d).

To describe the phase transition, we plotted averaged concentration of the extracted components as a function of the temperature (laser power) (Fig. 6a). As one can see, the concentrations of the third and second components demonstrate behavior typical for a phase transition – *i.e.* decreasing of the third component concentration is accompanied by a concomitant increase of the second one. Observed monotonic decrease of the first component concentration probably reflects change of the properties in $In_{4/3}P_2S_6$ phase.

However, extraction of the critical laser power corresponding to the ferroelectric-paraelectric phase transition is hampered by the spatial temperature inhomogeneity in the heated region. Indeed, the acquired Raman signal is averaged over the 500 nm-sized region containing

both ferroelectric and paraelectric phases in the critical regime. Precise extraction of the critical power requires the unknown distribution of the optical signal. Thus, here we use an approximated value, $P_{0.77}^{C} = 720\mu W$, corresponding to equal concentrations of the ferroelectric and paraelectric phases in the probing volume (Fig. 7a).

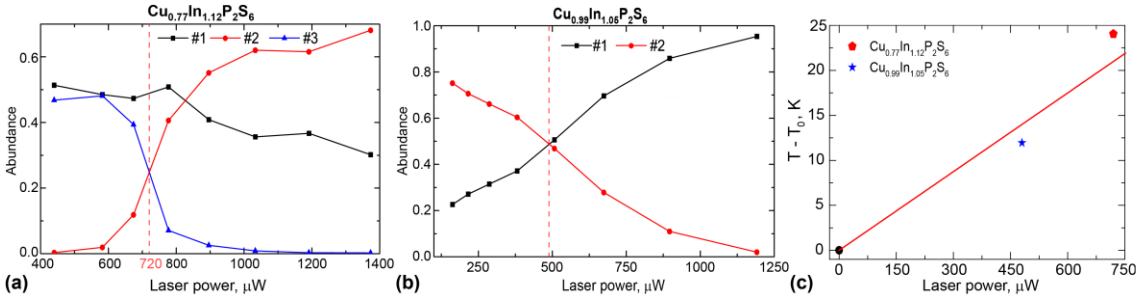

Figure 7. (a-b) Components concentration averaged over same laser power for $Cu_{0.77}In_{1.12}P_2S_6$ (a) and $Cu_{0.99}In_{1.05}P_2S_6$ (b) samples. (c) Calibration plot of temperature vs laser power.

Note that the simulation demonstrated a linear relationship between the laser power and temperature. To establish this, we looked at the second $Cu_{0.99}In_{1.05}P_2S_6$ sample (Supplemental materials, Fig. S5-S6). Investigations revealed a critical laser power of $P_{0.99}^{C} = 480\mu W$ (Fig. 7b). These results are consistent with Curie temperatures data for both samples (Fig. 7c). Obtained experimental results along with known values of the Curie temperatures for studied samples allowed temperature calibration: $T = T_0 + \beta P_{laser}$, where T_0 is room temperature and β is the conversion factor (Fig. 7c). Estimations for both studied samples gave reasonably close β values: $\beta_{0.77}$ = 33.4 mK/μW and $\beta_{0.99}$ = 24.9 mK/μW. These data highlight the reproducibility of our results and underpin the applicability of the developed technique for wider range of materials and applications.

In addition performed computer simulation with known material constants, the critical laser power and Curie temperature allowed us to estimate the laser heat "efficiency" factor $\alpha = 0.15$ with simulated spot size about $R_{spot} = 2$ μm. Such a small value of the adsorption factor is not surprising as studied ferroelectric CIPS exhibit large band-gaps and thus are transparent to the pumped laser wavelength used in this study (532 nm).

Conclusion

We introduced a fast local heating technique for functional imaging in scanning probe microscopy. The laser irradiation induces heating in the region much larger than typical SPM probing volume, which allows mapping in an effectively uniform temperature field. The suggested technique has been applied to the layered ferroelectrics of copper indium thiophosphate for investigation of the ferroelectric-paraelectric phase transition. The in-situ measurements by Piezoresponse force microscopy and confocal micro-Raman spectroscopy revealed correlated changes in the domain structure and Raman spectra. These data were used as a sign of the transition from ferroelectric to paraelectric phase for further temperature calibration.

However, non-polar inclusions of $In_{4/3}P_2S_6$ hampered direct identification of the phase transformation. The problem was resolved using Bayesian linear unmixing and principal component analysis for the separation of the Raman spectra corresponding to different material phases. These results, along with the independently measured Curie temperatures and finite element simulation of the temperature distribution, allowed us to calibrate the temperature in the irradiated region close to the tip.

These results are important for the development of novel SPM techniques and enable a systematic approach for studying temperature dependent material functionalities in previously inaccessible temperature regimes.

Methods

As model systems with well-defined temperature-dependent functionalities we have chosen two copper indium thiophosphate samples (CIPS): $Cu_{0.77}In_{1.12}P_2S_6$ and $Cu_{0.99}In_{1.05}P_2S_6$, with Curie temperatures of the ferroelectric-paralectric phase transition $T_{0.77}^{C} = 320K$ and $T_{0.99}^{C} = 308K$, respectively.[38] Measurements have been performed using an Ntegra Spectra (NT-MDT, Russia) combined scanning probe microscope with confocal Raman spectrometer This allowed simultaneous PFM and micro-Raman measurements.

Acknowledgements

A portion of this research (AVI and SVK) was conducted at the Center for Nanophase Materials Sciences, which is a DOE Office of Science User Facility. Samples growth and preparation (PM, MAS and MAM) were sponsored by the Laboratory Directed Research and Development program at the Oak Ridge National Laboratory.

Supporting information available: detailed results of investigations in $Cu_{0.99}In_{1.05}P_2S_6$ sample; detailed description of principal component analysis and its application for data processing. This material is available free of charge *via* the Internet at http://pubs.acs.org.

References

1 Binnig, G. K. Atomic-Force Microscopy. *Phys. Scr.* **T19A**, 53-54 (1987).

2 Baselt, D. R. & Baldeschwieler, J. D. Imaging Spectroscopy with the Atomic Force Microscope. *J. App. Phys.* **76**, 33-38 (1994).

3 Rabe, U. & Arnold, W. Acoustic Microscopy by Atomic Force Microscopy. *Appl. Phys. Lett.* **64**, 1493-1495 (1994).

4 Cantrell, S. A., Cantrell, J. H. & Lillehei, P. T. Nanoscale Subsurface Imaging *via* Resonant Difference-Frequency Atomic Force Ultrasonic Microscopy. *J. App. Phys.* **101**, 114324 (2007).

5 Nonnenmacher, M., Oboyle, M. P. & Wickramasinghe, H. K. Kelvin Probe Force Microscopy. *Appl. Phys. Lett.* **58**, 2921-2923 (1991).

6 Jacobs, H. O., Leuchtmann, P., Homan, O. J. & Stemmer, A. Resolution and Contrast in Kelvin Probe Force Microscopy. *J. App. Phys.* **84**, 1168-1173 (1998).

7 Stern, J. E., Terris, B. D., Mamin, H. J. & Rugar, D. Deposition and Imaging of Localized Charge on Insulator Surfaces Using a Force Microscope. *Appl. Phys. Lett.* **53**, 2717-2719 (1988).

8 Schönenberger, C. & Alvarado, S. F. Observation of Single Charge Carriers by Force Microscopy. *Phys. Rev. Lett.* **65**, 3162-3164 (1990).

9 Seidel, J., Martin, L. W., He, Q., Zhan, Q., Chu, Y. H., Rother, A., Hawkridge, M. E., Maksymovych, P., Yu, P., Gajek, M. *et al.* Conduction at Domain Walls in Oxide Multiferroics. *Nat. Mater.* **8**, 229-234 (2009).

10 Strelcov, E., Belianinov, A., Hsieh, Y.-H., Jesse, S., Baddorf, A. P., Chu, Y.-H. & Kalinin, S. V. Deep Data Analysis of Conductive Phenomena on Complex Oxide Interfaces: Physics from Data Mining. *ACS Nano* **8**, 6449-6457 (2014).

11 Gruverman, A., Auciello, O., Ramesh, R. & Tokumoto, H. Scanning Force Microscopy of Domain Structure in Ferroelectric Thin Films: Imaging and Control. *Nanotechnology* **8**, A38-A43 (1997).

12 Gruverman, A., Auciello, O. & Tokumoto, H. Imaging and Control of Domain Structures in Ferroelectric Thin Films *via* Scanning Force Microscopy. *Annu. Rev. Mater. Sci.* **28**, 101-123 (1998).

13 Soergel, E. Piezoresponse Force Microscopy (PFM). *J. Phys. D-Appl. Phys.* **44**, 464003 (2011).

14 Kalinin, S. V., Morozovska, A. N., Chen, L. Q. & Rodriguez, B. J. Local Polarization Dynamics in Ferroelectric Materials. *Rep. Prog. Phys.* **73**, 056502 (2010).

15 Majumdar, A. Scanning Thermal Microscopy. *Annu. Rev. Mater. Sci.* **29**, 505-585 (1999).

16 Nonnenmacher, M. & Wickramasinghe, H. K. Scanning Probe Microscopy of Thermal Conductivity and Subsurface Properties. *Appl. Phys. Lett.* **61**, 168-170 (1992).

17 Binnig, G., Despont, M., Drechsler, U., Häberle, W., Lutwyche, M., Vettiger, P., Mamin, H. J., Chui, B. W. & Kenny, T. W. Ultrahigh-Density Atomic Force Microscopy Data Storage with Erase Capability. *Appl. Phys. Lett.* **74**, 1329-1331 (1999).

18 Kalinin, S. V. & Bonnell, D. A. Temperature Dependence of Polarization and Charge Dynamics on the $BaTiO_3$(100) Surface by Scanning Probe Microscopy. *Appl. Phys. Lett.* **78**, 1116-1118 (2001).

19 Leib, J., Snyder, J. E., Lo, C. C. H., Paulsen, J. A., Xi, P. & Jiles, D. C. Magnetic Force Microscopy Characterization of a First-Order Transition: Magnetic-Martensitic Phase Transformation in $Gd_5(Si_xGe_{1-X})_4$. *J. App. Phys.* **91**, 8852-8854 (2002).

20 Lemieux, M., Minko, S., Usov, D., Stamm, M. & Tsukruk, V. V. Direct Measurement of Thermoelastic Properties of Glassy and Rubbery Polymer Brush Nanolayers Grown by "Grafting-from" Approach. *Langmuir* **19**, 6126-6134 (2003).

21 Onoue, T., Siekman, M. H., Abelmann, L. & Lodder, J. C. Heat-Assisted Magnetic Probe Recording on a CoNi/Pt Multilayered Film. *J. Magn. Magn. Mater.* **287**, 501-506 (2005).

22 Shvartsman, V. V., Kleemann, W., Dec, J., Xu, Z. K. & Lu, S. G. Diffuse Phase Transition in $BaTi_{1-x}Sn_xO_3$ Ceramics: An Intermediate State between Ferroelectric and Relaxor Behavior. *J. App. Phys.* **99**, 8 (2006).

23 Wang, Z. L., Tang, D. W., Li, X. B., Zheng, X. H., Zhang, W. G., Zheng, L. X., Zhu, Y. T., Jin, A. Z., Yang, H. F. & Gu, C. Z. Length-Dependent Thermal Conductivity of an Individual Single-Wall Carbon Nanotube. *Appl. Phys. Lett.* **91**, 123119 (2007).

24 Shvartsman, V. V. & Kholkin, A. L. Evolution of Nanodomains in $0.9PbMg_{1/3}Nb_{2/3}O_3$-$0.1PbTiO_3$ Single Crystals. *J. App. Phys.* **101**, 5 (2007).

25 Nikiforov, M. P., Jesse, S., Morozovska, A. N., Eliseev, E. A., Germinario, L. T. & Kalinin, S. V. Probing the Temperature Dependence of the Mechanical Properties of Polymers at the Nanoscale with Band Excitation Thermal Scanning Probe Microscopy. *Nanotechnology* **20** (2009).

26 Shi, L., Zhou, J. H., Kim, P., Bachtold, A., Majumdar, A. & McEuen, P. L. Thermal Probing of Energy Dissipation in Current-Carrying Carbon Nanotubes. *J. App. Phys.* **105**, 5 (2009).

27 Groten, J., Zirkl, M., Jakopic, G., Leitner, A. & Stadlober, B. Pyroelectric Scanning Probe Microscopy: A Method for Local Measurement of the Pyroelectric Effect in Ferroelectric Thin Films. *Phys. Rev. B* **82**, 11 (2010).

28 Pires, D., Hedrick, J. L., De Silva, A., Frommer, J., Gotsmann, B., Wolf, H., Despont, M., Duerig, U. & Knoll, A. W. Nanoscale Three-Dimensional Patterning of Molecular Resists by Scanning Probes. *Science* **328**, 732-735 (2010).

29 Shur, V. Y., Mingaliev, E. A., Lebedev, V. A., Kuznetsov, D. K. & Fursov, D. V. Polarization Reversal Induced by Heating-Cooling Cycles in MgO Doped Lithium Niobate Crystals. *J. App. Phys.* **113** (2013).

30 Ievlev, A. V., Jesse, S., Morozovska, A. N., Strelcov, E., Eliseev, E. A., Pershin, Y. V., Kumar, A., Shur, V. Y. & Kalinin, S. V. Intermittency, Quasiperiodicity and Chaos in Probe-Induced Ferroelectric Domain Switching. *Nat. Phys.* **10**, 59-66 (2014).

31 Dahan, D., Molotskii, M., Rosenman, G. & Rosenwaks, Y. Ferroelectric Domain Inversion: The Role of Humidity. *Appl. Phys. Lett.* **89**, 152902 (2006).

32 Ievlev, A. V., Morozovska, A. N., Shur, V. Y. & Kalinin, S. V. Humidity Effects on Tip-Induced Polarization Switching in Lithium Niobate. *Appl. Phys. Lett.* **104**, 092908 (2014).

33 Schenk, M., Füting, M. & Reichelt, R. Direct Visualization of the Dynamic Behavior of a Water Meniscus by Scanning Electron Microscopy. *J. App. Phys.* **84**, 4880-4884 (1998).

34 Ievlev, A. V., Morozovska, A. N., Eliseev, E. A., Shur, V. Y. & Kalinin, S. V. Ionic Field Effect and Memristive Phenomena in Single-Point Ferroelectric Domain Switching. *Nat. Comm.* **5**, 5545 (2014).

35 Maisonneuve, V., Cajipe, V. B., Simon, A., Von Der Muhll, R. & Ravez, J. Ferrielectric Ordering in Lamellar $CuInP_2S_6$. *Phys. Rev. B* **56**, 10860-10868 (1997).
36 Vysochanskii, Y. M., Stephanovich, V. A., Molnar, A. A., Cajipe, V. B. & Bourdon, X. Raman Spectroscopy Study of the Ferrielectric-Paraelectric Transition in Layered $CuInP_2S_6$. *Phys. Rev. B* **58**, 9119-9124 (1998).
37 Belianinov, A., He, Q., Dziaugys, A., Maksymovych, P., Eliseev, E., Borisevich, A., Morozovska, A., Banys, J., Vysochanskii, Y. & Kalinin, S. V. Cuinp2s6 Room Temperature Layered Ferroelectric. *Nano Lett.* **15**, 3808-3814 (2015).
38 Susner, M. A., Belianinov, A., Borisevich, A. Y., Qian, H., Panchapakesan, G., Hakan, D., Sholl, D. S., Douglas, L. A., McGuire, M. A. & Maksymovych, P. High Tc Layered Ferrielectric Crystals by Coherent Spinodal Decomposition. *ACS Nano* ((submitted)).
39 Balandin, A. A., Ghosh, S., Bao, W. Z., Calizo, I., Teweldebrhan, D., Miao, F. & Lau, C. N. Superior Thermal Conductivity of Single-Layer Graphene. *Nano Lett.* **8**, 902-907 (2008).
40 Périchon, S., Lysenko, V., Remaki, B., Barbier, D. & Champagnon, B. Measurement of Porous Silicon Thermal Conductivity by Micro-Raman Scattering. *J. App. Phys.* **86**, 4700-4702 (1999).
41 Vlassiouk I., Smirnov S., Ivanov I., Fulvio P.F., Dai S., Ch M., Hansley D., Datskos P. & Lavrik N.V. Electrical and Thermal Conductivity of Low Temperature CVD Graphene: The Effect of Disorder. *Nanotechnology* **22**, 275716 (2011).
42 Andersson, O., Chobal, O., Rizak, I., Rizak, V. & Sabadosh, V. Effects of Pressure and Temperature on the Thermal Conductivity of $Sn_2P_2S_6$. *Phys. Rev. B* **83**, 134121 (2011).
43 Dobigeon, N., Moussaoui, S., Coulon, M., Tourneret, J.-Y. & Hero, A. O. Joint Bayesian Endmember Extraction and Linear Unmixing for Hyperspectral Imagery. *IEEE Trans. Signal Proces.* **57**, 4355-4368 (2009).
44 Dobigeon, N. & Brun, N. Spectral Mixture Analysis of Eels Spectrum-Images. *Ultramicroscopy* **120**, 25-34 (2012).
45 Jesse, S. & Kalinin, S. V. Principal Component and Spatial Correlation Analysis of Spectroscopic-Imaging Data in Scanning Probe Microscopy. *Nanotechnology* **20**, 085714 (2009).
46 Bonnet, N. Multivariate Statistical Methods for the Analysis of Microscope Image Series: Applications in Materials Science. *J. Microsc. (Oxford U.K.)* **190**, 2-18 (1998).
47 Belianinov, A., Vasudevan, R., Strelcov, E., Steed, C., Yang, S., Tselev, A., Jesse, S., Biegalski, M., Shipman, G., Symons, C. *et al.* Big Data and Deep Data in Scanning and Electron Microscopies: Deriving Functionality from Multidimensional Data Sets. *Adv Struct Chem. Imag.* **1**, 1-25 (2015).